A numerical study on ripple evolution and migration using a two-phase flow model

A. Salimi-Tarazouj *Center for Applied Coastal Research, University of Delaware, USA – alisalim@udel.edu*
T.J. Hsu *Center for Applied Coastal Research, University of Delaware, USA – thsu@udel.edu*
P. Traykovski *Woods Hole Oceanographic Institution, USA – ptraykovski@whoi.edu*
J. Chauchat *LEGI, University of Grenoble Alpes, France – julien.chauchat@univ-grenoble-alpes.fr*

ABSTRACT: The evolution of ripple geometries and their equilibrium states due to different wave forcing parameters are investigated by a Reynolds-averaged two-phase model, SedFoam, in a two-dimensional domain. Modeled ripple geometries, for a given uniform grain diameter, show a good agreement with ripple predictors that include the wave period effect explicitly, in addition to the wave orbital excursion length (or wave orbital velocity amplitude).

1 INTRODUCTION

Oscillatory flow motions of surface wave near seabed can generate a wide range of bedforms. Bedforms are essential due to their effect on the seabed roughness and wave-current driven onshore/offshore sediment transport. Field and laboratory observation on onshore/offshore sediment transport in orbital ripple regime suggested that under onshore velocity skewed waves, suspended load above the ripple was offshore directed while onshore transport occurred as ripple migration. These complex processes associated with suspended load and ripple migration pose a challenge to conventional single-phased sediment transport models as they require assumptions and empirical treatments in modeling suspended load and bedload. We present a novel numerical model that is able to resolve sediment transport over ripples and ripple migration altogether in a Eulerian two-phase modeling framework, called SedFoam. With a two-equation k-epsilon closure, interphase drag and particle stresses, the model can resolve full profiles of sediment concentration and particle/fluid velocities. Particularly, a careful consideration of particle stresses in the high concentration of fluid-solid transition is essential to the resulting ripple steepness and migration speed.

2 GOVERNING EQUATIONS AND NUMERICAL MODEL

The two-phase model sedFoam (Chauchat et al. 2017) (https://github.com/SedFoam/sedfoam) is used to simulate the formation and evolution of ripples in oscillatory flows using the Reynolds-averaged k-ε turbulence model.

In the Eulerian two-phase flow formalism, coupled mass and momentum conservation equations for the fluid and the solid phases are solved. The mass conservation for the fluid and the solid phase are given by

$$\frac{\partial(1-\phi)}{\partial t} + \frac{\partial(1-\phi)u_i^f}{\partial x_i} = 0 \tag{1}$$

$$\frac{\partial \phi}{\partial t} + \frac{\partial \phi u_i^s}{\partial x_i} = 0 \tag{2}$$

respectively with x the position vector, $i = 1,2,3$ representing the streamwise, vertical and spanwise components, ϕ the filtered sediment concentration and u^f and u^s the fluid and solid Favre filtered velocities.

The fluid and solid momentum conservation equation are written as

$$\frac{\partial \rho^f (1-\phi)u_i^f}{\partial t} + \frac{\partial \rho^f (1-\phi)u_i^f u_j^f}{\partial x_j} =$$
$$-(1-\phi)\frac{\partial P^f}{\partial x_i} + \frac{\partial}{\partial x_i}\left[T_{ij}^f\right]$$
$$-I_i + \rho^f (1-\phi)g_i + (1-\phi)f_i^v \tag{3}$$

$$\frac{\partial \rho^s \phi u_i^f}{\partial t} + \frac{\partial \rho^s \phi u_i^s u_j^s}{\partial x_j} = -\phi \frac{\partial P^f}{\partial x_i} - \frac{\partial P^s}{\partial x_i}$$

$$\frac{+\partial}{\partial x_i}\left[T_{ij}^s\right] + I_i + \rho^s \phi g_i + \phi f_i^v$$

(4)

with ρ^f and ρ^s the fluid and solid densities and P^f and P^s the fluid ans solid phase pressures. The effective fluid and solid stress tensors T^f and T^s are given by

$$T_{ij}^f = \rho^f(1-\phi)\nu^f\left(\frac{\partial u_j^f}{\partial x_i} + \frac{\partial u_i^f}{\partial x_j} - \frac{2}{3}\frac{\partial u_k^f}{\partial x_k}\delta_{ij}\right) \quad (5)$$

$$T_{ij}^s = \rho^s \phi \nu^s\left(\frac{\partial u_j^s}{\partial x_i} + \frac{\partial u_i^s}{\partial x_j} - \frac{2}{3}\frac{\partial u_k^s}{\partial x_k}\delta_{ij}\right) \quad (6)$$

where ν^f and ν^s are the fluid and solid phases viscosities, g is the acceleration of gravity and f^v a volume force driving the flow.

The momentum exchange term between the two phases I is modelled using the semi-empirical drag law from Ding and Gidaspow (1990). The interested reader is referred to Chauchat *et al.* (2017) for more details about the model and the closures.

3 RESULTS AND DISCUSSION

Figure 1 shows the typical domain characteristics and boundary conditions. At the top domain boundary, a free-slip (i.e., Neumann) boundary condition is used for both the fluid and sediment field quantities. At the bottom boundary, a no-slip boundary is used for the velocities of both phases while a zero-gradient boundary is used for the other quantities. For the pressure field, a fixed zero value is specified at the top

boundary, and at the bottom boundary of the domain, a zero gradient condition is imposed. Periodic boundary conditions are specified at the two lateral boundaries to minimize computational domain length and Lx i is set to be the same as the measured equilibrium ripple reported by van der Werf et al. (2007). The domain length specified such that it includes n = 3 ripples. For initial ripple height η_i, we specify a much larger value than that measured ripple height. The domain height is set to be Lz = 0.5 m in all the simulations.

The oscillatory flow is driven by a prescribed horizontal pressure gradient which generates a free-stream velocity time series following the Stokes second-order wave.

In table 1, four cases are presented corresponding to different wave forcing conditions and the same sand diameter (d$_{50}$=440 μm, s=ρ_s/ ρ_f =2.65). The ripple profile at different wave cycle is shown in figure 2 a for case 1, the ripple height slightly reduces and the ripple migrates onshore. By tracking the position of the ripples crest it is possible to deduce the migration speed of the ripple which is shown in figure 2b for case 1 and 2. The numerical model predicts no migration for the symmetric wave case 2 (as expected) and a migration rate of 14-15 mm/min for case 1 which is very comparable with the measured value of 18 mm/min by van der Werf *et al.* (2007). This first result validate the two-phase flow approach for simulation of ripple migration by asymmetric waves. More details can be found in Salimi-Tarazouj *et al.* (2021a).
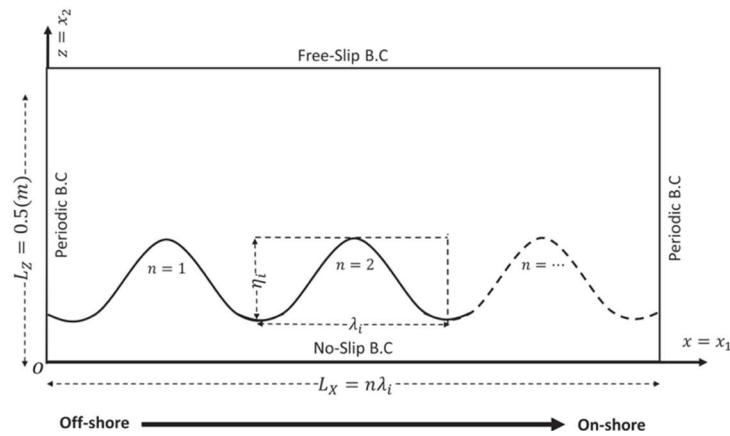

Figure 1: Schematic plot of the model domain and initial ripple bed profile

Table 1: Parameters for numerical configurations

Case #	Waves (order)	T (s)	U_m (m/s)	λ_e (m)	η_e/λ_e (-)
1	2nd	5	0.54	0.41	0.19
2	1st	5	0.48	0.46	0.17
3	1st	3	0.48	0.23	0.17
4	1st	3	0.8	0.345	0.13

The morphodynamical evolution of the ripple is the result of the small imbalance in the sediment fluxes during a wave period. Figure 3 and 4 show the period-averaged dimensionless vorticity field (Ω/ω) and the dimensionless sediment flux (ψ).
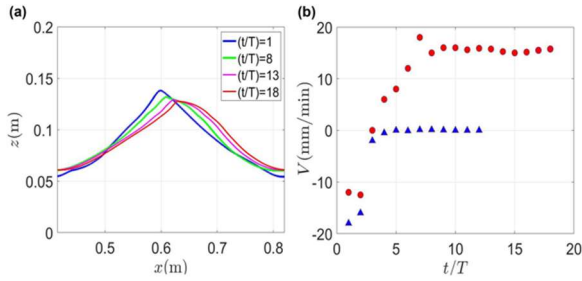

Figure 2: (a) Ripple profile for the middle ripple in Case 1 at different wave cycle. (b) Ripple migration rate as a function of the number of wave's cycle for the middle ripple in Case 1 (red circles) and Case 2 (blue triangles).
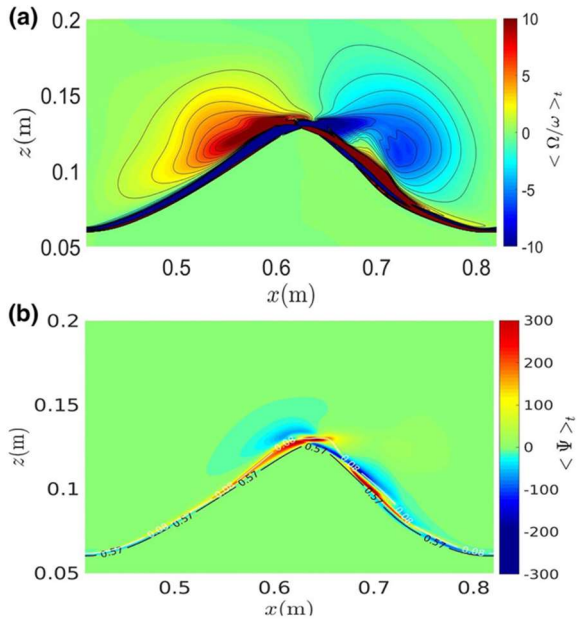

Figure 3: (a) Wave-period-averaged normalized vorticity (color-bar) for Case 1. Panel (b) shows the corresponding wave-period-averaged normalized sediment horizontal flux.
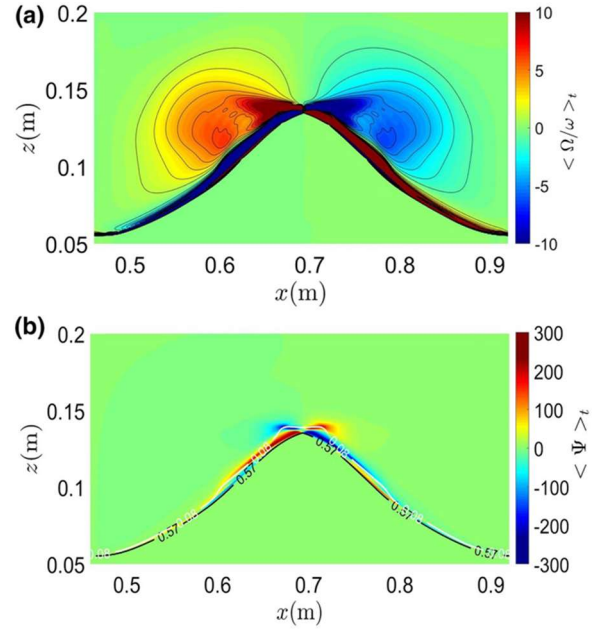

Figure 4: idem as figure 3 for case 2.

While the vorticity field and the sediment flux are symmetric in case 2 (figure 4, sinusoidal wave) a slight asymmetry is observed in case 1 (figure 3, 2nd order Stokes wave) which shows a larger primary vortex at the onshore side of the ripple (negative/clockwise vorticity), reflecting the stronger onshore flow driven by onshore velocity-skewed wave motion. This asymmetry generates an intense, offshore directed flow close to the onshore side of the ripple's surface and ripple crest which lead to a larger onshore transport via near-bed load. This the key mechanism by which the ripple migrates.

In figure 5, the space-time diagram of the bed elevation for case 3 and 4 are shown. This figure illustrates the model's capability to simulate the reduction and increase of ripple length and height due to two scenarios. The simulation is initialized with three orbital ripples in the domain resulted from a 5 sec wave of orbital velocity 0.48 m/s (case 2). In the first scenario (Figure 5a), we reduce the period to 3 sec and hence the orbital length is also reduced. This causes three large ripples to first split and then merge into 6 smaller ripples. In the second scenario, we increase the orbital velocity to 0.8 m/s and three large orbital ripples evolve into four smaller sub-orbital ripples via merging and sliding (Figure 5b). The interested reader is referred to
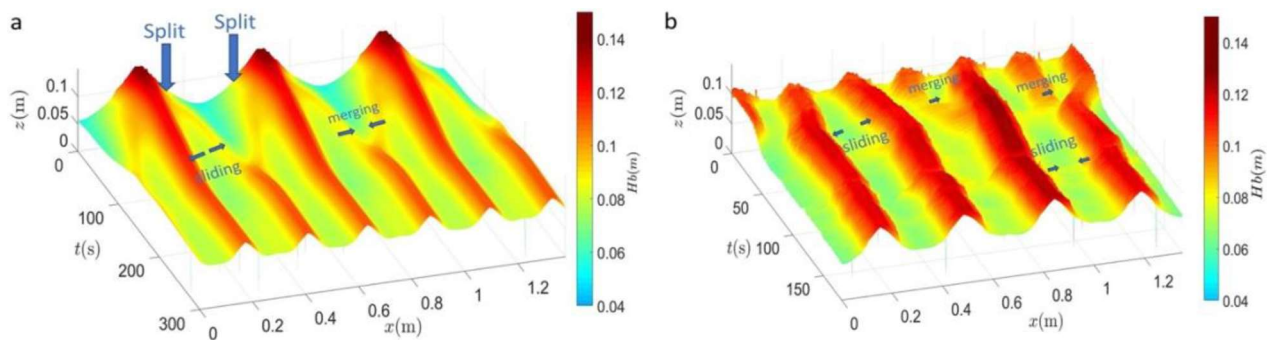
Figure 5: Time series of ripple bed evolution for case 3 (a) and case 4 (b)

Salimi-Tarazouj et al. (2021b) for more details about the effect of wave period on the ripple characteristics.

4 CONCLUSION

In this contribution we demonstrated the capabilities of the two-phase flow modeling approach to simulate the evolution and migration of ripples generated by an oscillatory flow. The model has been validated using experimental data and through a series of numerical experiments, the ripple's response to a step-change in the wave forcing has been studied. The model is capable of simulating "splitting", "sliding", "merging", and "protruding" as the ripples evolve to a new equilibrium state.

The model can also simulate the transition to sheet flow in energetic wave conditions and ripple reformation from a nearly flat bed condition. Simulation results reveal that the equilibrium state is such that the "primary" vortices reach half of the ripple length. Furthermore, an analysis of the suspended load and near-bed load ratio in the equilibrium state indicates that in the orbital ripple regime, the near-bed load is dominant while the suspended load is conducive to the ripple decaying regime (suborbital ripples) and sheet flow condition.

5 REFERENCES

Chauchat, J., Cheng, Z., Nagel, T., Bonamy, C., Hsu, T.-J., 2017. SedFoam-2.0: a 3-D two-phase flow numerical model for sediment transport 105194, 4367–4392. https://doi.org/10.5194/gmd-10-4367-2017

Ding, J., & Gidaspow, D. (1990). A bubbling fluidization model using kinetic theory of granular flow. AIChE Journal, 36(4), 523–538. https://doi.org/10.1002/aic.690360404

Johnson, P.C., Jackson, R., 1987. Frictional–collisional constitutive relations for granular materials, with application to plane shearing. Journal of Fluid Mechanics, 176, 67-93. doi:10.1017/S0022112087000570

Traykovski, P., Hay, A.E., Irish, J.D., Lynch, J.F., 1999. Geometry, migration, and evolution of wave orbital ripples at LEO-15. J. Geophys. Res. Ocean. 104, 1505–1524. https://doi.org/10.1029/1998JC900026

Salimi-Tarazouj, A., Hsu, T.-J., Traykovski, P., Cheng, Z., & Chauchat, J. (2021a). A numerical study of onshore ripple migration using a Eulerian two-phase model. Journal of Geophysical Research: Oceans, 126, e2020JC016773. https://doi.org/10.1029/2020JC016773

Salimi-Tarazouj, A., Hsu, T.-J., Traykovski, P., & Chauchat, J. (2021b). Eulerian two-phase model reveals the importance of wave period in ripple evolution and equilibrium geometry. Journal of Geophysical Research: Earth Surface, 126, e2021JF006132. https://doi.org/10.1029/2021JF006132

van der Werf, J. J., Doucette, J. S., O'Donoghue, T., & Ribberink, J. S. (2007). Detailed measurements of velocities and suspended sand concentrations over full-scale ripples in regular oscillatory flow. Journal of Geophysical Research, 112(2), 1–18. https://doi.org/10.1029/2006JF000614

Hydrodynamical regimes in turbulent flows over a wavy surface and dissolution instability

P. Claudin   *Physique et Mécanique des Milieux Hétérogènes, PMMH UMR 7636 CNRS, ESPCI Paris, PSL Research University, Université Paris Cité, Sorbonne Université, Paris, France – philippe.claudin@espci.fr*
B. Andreotti   *Laboratoire de Physique de L'Ecole Normale Supérieure, UMR 8550 CNRS, PSL Research University, Université Paris Cité, Sorbonne Université, Paris, France*

ABSTRACT: We theoretically investigate the pattern formation observed when a fluid flows over a solid substrate that can dissolve, melt or sublimate. We use a turbulent mixing description that includes the effect of the bed roughness. We show that the dissolution instability at the origin of the pattern that emerges is associated with an anomaly at the transition from a laminar to a turbulent hydrodynamic response with respect to the bed elevation. This anomaly, and therefore the instability, disappears when the bed becomes hydrodynamically rough.

1 INTRODUCTION

We are interested in pattern formation associated with a fluid flow over a solid bed, when mass transfer has a thermodynamic origin with melting, sublimation or dissolution of the bed. Figure 1 shows a typical example of scallops forming in limestone, in a river bed. The flow is influenced by the bed elevation and, in turn, erosion or transport induced by the flow makes the solid surface evolve. This feedback loop can lead to an unstable situation, where bed perturbations are amplified. Several linear stability analyses have been performed for these dissolution/melting problems, in order to compute the growth rate of a perturbation of given wavenumber k and determine the most unstable mode (Hanratty, 1981). In this presentation, we show that taking into account the bed roughness in the hydrodynamic description is of key importance as the dissolution instability is found to disappear when the bed becomes rough. Section 2 briefly summarizes the hydrodynamic model. Section 3 presents the stability analysis. Section 4 shows the main results and concludes. More details can be found in Claudin et al. (2017).

Figure 1. Centimeter-scale scallops in limestone on Ardèche river (France).

2 HYDRODYNAMIC MODEL

We consider a flow in the horizontal x-direction. The axis z is vertical. We use RANS equations to solve for the velocity u_i and pressure p fields. The stress tensor τ_{ij} is related to the strain rate $\dot{\gamma}_{ij} = \partial_i u_j + \partial_j u_i$ by means of a turbulent closure that involves a mixing length ℓ. In order to account for both smooth and rough regimes, we adopt here a van Driest-like expression for it:

$$\ell = \kappa(z + rd) \times \left[1 - \exp\left(-\frac{(z+sd)(\tau_{xz}/\rho)^{1/2}}{\nu \mathcal{R}_t}\right)\right]$$
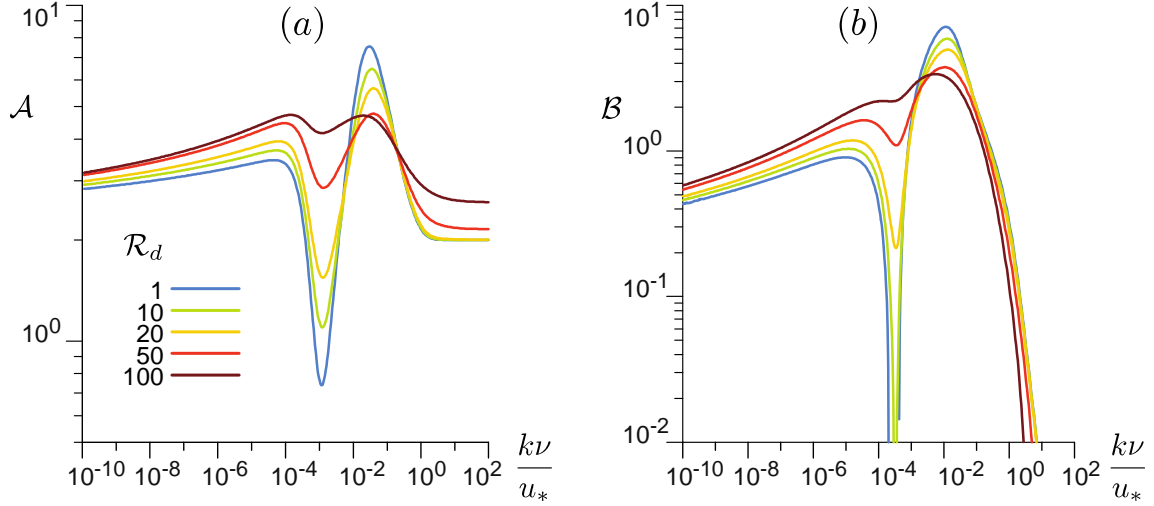
Figure 2. Basal shear stress coefficients $\mathcal{A}$ (a) and $\mathcal{B}$ (b) computed by the model as functions of kv/u_*. The different colors code for the value of the bed roughness Reynolds number $\mathcal{R}_d$ (legend). The laminar–turbulent transition (around $kv/u_* \simeq 10^{-3}$) gradually disappears when $\mathcal{R}_d$ increases.

In this expression, $\kappa \simeq 0.4$ is the von Kármán constant, z is the distance to the bed, d is the sand equivalent bed roughness size, v is the kinematic viscosity of the fluid, ρ is its mass density. $\mathcal{R}_t$ is the van Driest transitional Reynolds number, equal to $\mathcal{R}_t^0 \simeq 25$ in the homogeneous case of a flat bed. The exponential term suppresses turbulent mixing within the viscous sub-layer, close enough to the bed. The dimensionless numbers r and s are calibrated with measurements of velocity profiles over varied rough walls (see Claudin et al. (2017) and refs therein).

Following Hanratty (1981), $\mathcal{R}_t$ cannot be taken as a constant, but instead lags behind the pressure gradient by a space lag on the order of v/u_* that is associated with a thickening of the boundary layer. We then write for $\mathcal{R}_t$ the spatial relaxation equation

$$a \frac{v}{u_*} \partial_x \mathcal{R}_t = b \frac{v \mathcal{R}_t^0}{\rho u_*^3} \partial_x (\tau_{xx} - p)$$
$$- (\mathcal{R}_t - \mathcal{R}_t^0) \qquad (2)$$

where the constants a and b have been calibrated by Charru et al. (2013) on experimental data (Zilker et al., 1977; Frederick et al., 1988).

These data report measurements of the basal shear stress when the flow is perturbed by a sinusoidal bed $Z(x) = \zeta e^{ikx}$ (NB: we use complex notations for compactness, real parts are understood). At the linear order in $k\zeta$, the shear stress is also modulated and takes the generic form $\tau_{xz} = \rho u_*^2 [1 + k\zeta e^{ikx} S_t]$. The mode function S_t depends on the dimensionless height kz. We define the two coefficients $\mathcal{A}$ and $\mathcal{B}$ by $S_t(0) = \mathcal{A} + i\mathcal{B}$. They encode the in-phase and in-quadrature stress linear response to the bed perturbation. They are computed by the hydrodynamic model, and their dependence on kv/u_* if displayed in Fig. 2 for various values of $\mathcal{R}_d = du_*/v$. In the smooth limit (small $\mathcal{R}_d$), they show a marked transition between the turbulent regime associated with small wavenumbers $kv/u_* < 10^{-4}$ and the laminar regime, typically for $kv/u_* > 10^{-2}$. This `anomaly' at the laminar-turbulent transition, around $kv/u_* \simeq 10^{-3}$, experimentally evidenced by Hanratty and coworkers, plays as crucial role in the dissolution instability. It also shows up for the basal pressure response (Claudin et al., 2021), as well as for the effective topography -induced hydrodynamic roughness (Jia et al., 2023). Importantly, it disappears in the rough regime (Fourrière et al., 2010), for large enough $\mathcal{R}_d \gtrsim 100$.

3 LINEAR STABILITY ANALYSIS

We wish now to describe a passive scalar ϕ, e.g. the concentration of a chemical species or the temperature, which is transported by the flow. We model its dynamics by a simple advection–diffusion equation

$$\partial_t \phi + \vec{\nabla} \cdot \vec{q} = 0 \qquad (3)$$

where the flux $\vec{q}$ is the sum of a convective and a diffusive term $\vec{q} = \phi\vec{u} - D\vec{\nabla}\phi$. Here, we take a diffusion coefficient D proportional to the turbulent viscosity and write

$$D = \frac{v}{\beta_v} + \frac{\ell^2 \dot{\gamma}}{\beta_t} \qquad (4)$$

where $\dot{\gamma}$ is the modulus of the strain rate tensor. β_v (resp. β_t) is the viscous (resp. turbulent) Schmidt number (or Prandtl numbers for temperature), here taken as constants.

To perform the linear stability analysis of these equations, we write the bed profile as

$$Z(x,t) = \zeta e^{(\sigma+i\omega)t+ikx} \qquad (5)$$

where $\sigma(k)$ is the growth rate and $\omega(k)$ is the angular frequency of the bed pattern along x. The phase propagation speed is therefore $-\omega/k$. The equations of the model are linearized with respect to $k\zeta$ and can be solved with suitable boundary conditions. All components of their solution are written in the form of a correction to the base state (the flat case $k\zeta = 0$, homogeneous in x), proportional to kZ times a mode function. The evolution equation of the bed can be written as

$$\partial_t Z = q_0 - q_z(Z) \qquad (6)$$

where $q_0 = \alpha(\phi_{sat} - \phi_0)$ is the scalar flux in the base state. The corresponding dispersion relation reads

$$\sigma + i\omega = q_0 k F(0) \qquad (7)$$

where F is the mode function associated with the flux correction. This function is related to the hydrodynamic fields (see Claudin et al. 2017 for details).
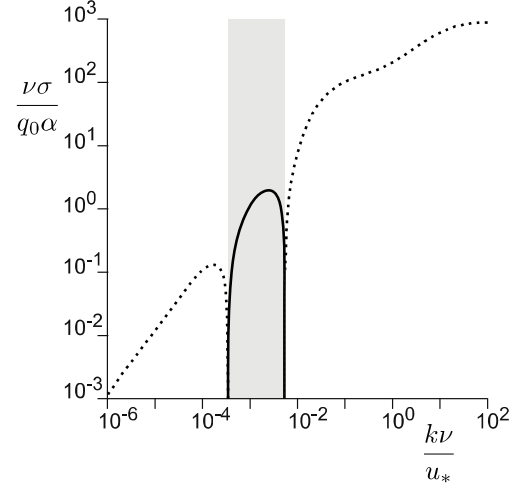

Figure 3. Dimensionless growth rate as a function of $k v/u_*$ in the limit of small α/u_* and for $\beta_v = 10^3$, $\mathcal{R}_d = 10$. Solid lines represent positive values. For negative values, $-\sigma$ is plotted (dotted lines). The grey region corresponds to the unstable ($\sigma > 0$) range of wavenumbers.
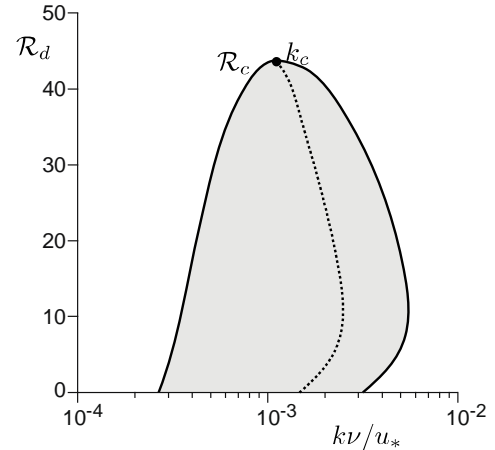

Figure 4. Stability diagram computed in the limit of small α/u_* and for $\beta_v = 10^3$. Solid line: marginal stability curve ($\sigma = 0$). Grey: unstable zone ($\sigma > 0$). Dotted line: location of the most unstable modes.

4 RESULTS AND CONCLUSIONS

The growth rate from (7) is displayed in Fig. 3, in the smooth case (small $\mathcal{R}_d$). We see a range of unstable wavenumbers with a positive growth rate, in which σ reaches a maximum value σ_m at k_m. As shown in Fig. 4, a key result is that the unstable band disappears above a critical value $\mathcal{R}_c$ of the roughness Reynolds number. This instability is governed by the laminar-turbulent transition, and is thus controlled by the

viscous length. An immediate robust result is that $k_m \propto u_*/v$ (with a prefactor on the order of 10^{-3}), a scaling law that is in good agreement with observations on various systems (Ashton & Kennedy, 1972; Blumberg & Curl, 1974; Curl, 1974; Thomas, 1979), including sublimation patterns on Mars (Bordiec et al., 2020).

One can understand the instability mechanism as follows. The erosion of the bed is driven by the mass flux itself controlled by the concentration gradient and the coefficient of diffusion. The concentration profile, enforced by the base state, is non-homogeneous, decreasing away from the surface. The crests of a modulated bed profile come closer to regions of lower concentration, enhancing the gradient with respect to the surface where ϕ is imposed. For a constant D, this peak effect increases the flux and thus the erosion at the crests, and this stabilising situation is what happens at large kv/u_*, when the wavelength is much smaller than the viscous sublayer. When turbulence is dominant, D is not constant any more, but is controlled by turbulent mixing. At small kv/u_*, turbulence is enhanced slightly upstream of the crests, and hence there is stabilizing erosion again. For wavenumbers in the intermediate range corresponding to the laminar–turbulent transition, however, turbulence is shifted downstream by means of the adverse pressure gradient (Eq. 2), enhancing mixing and thus erosion in the troughs, which is a destabilizing (amplifying) situation.

Further experimental studies, such as that of Bushuk et al. (2019), are needed to investigate the emergence and development of this instability in more detail, and in particular to follow the evolution of the bed roughness over time.

5 ACKNOWLEDGEMENT

6 REFERENCES

Ashton, G.D., Kennedy, J.F., 1972. Ripples on the underside of river ice covers. J. Hydraul. Div. ASCE 98, 1603.
doi:10.1061/JYCEAJ.0003407

Blumberg, P.N., Curl, R.L., 1974. Experimental and theoretical studies of dissolution roughness. J. Fluid Mech. 65, 735.
doi:10.1017/S0022112074001625

Bordiec, M., Carpy, S., Bourgeois, O., et al., 2020. Sublimation waves: Geomorphic markers of interactions between icy planetary surfaces and winds. Earth-Science Reviews 211, 103350.
doi:10.1016/j.earscirev.2020.103350

Bushuk, M., Holland, D.M., Stanton, T.P., Stern, A., Gray, C., 2019. Ice scallops: a laboratory investigation of the ice–water interface. J. Fluid Mech. 873, 942.
doi:10.1017/jfm.2019.398

Charru, F., Andreotti, B., Claudin, P., 2013. Sand ripples and dunes. Annu. Rev. Fluid Mech. 45, 469.
doi:10.1146/annurev-fluid-011212-140806

Claudin, P., Durán, O. Andreotti, B., 2017. Dissolution instability and roughening transition. J. Fluid Mech. 832, R2.
doi:10.1017/jfm.2017.711

Claudin, P., Louge, M., Andreotti, B., 2021. Basal pressure variations induced by a turbulent flow over a wavy surface. Front. Phys. 9, 682564.
doi: 10.3389/fphy.2021.682564

Curl, R.L., 1974. Deducing flow velocity in cave conduits from scallops. NSS Bull. 36, 1.

Fourrière, A., Claudin, P., Andreotti, B., 2010. Bedforms in a turbulent stream: formation of ripples by primary linear instability and of dunes by nonlinear pattern coarsening. J. Fluid Mech. 649, 287.
doi:10.1017/S0022112009993466

Frederick, K.A., Hanratty, T.J., 1988. Velocity measurements for a turbulent non-separated flow over solid waves. Exp. Fluids 6, 477.
doi:10.1007/BF00196509

Hanratty, T.J., 1981. Stability of surfaces that are dissolving or being formed by convective diffusion. Annu. Rev. Fluid Mech. 13, 231.
doi:10.1146/annurev.fl.13.010181.001311

Jia, P., Claudin, P., Andreotti, B., 2023. Topography-induced hydrodynamic roughness. Submitted.

Thomas, R.M., 1979. Size of scallops and ripples by flowing water. Nature 277, 281.
doi:10.1038/277281a0

Zilker, D.P., Cook, G.W., Hanratty, T.J., 1977. Influence of the amplitude of a solid wavy wall on a turbulent flow. Part 1. Non-separated flows. J. Fluid Mech. 82, 29.
doi:10.1017/S0022112077000524